NEUROSCIENCE

Small-molecule targeting AMPA-mediated excitotoxicity has therapeutic effects in mouse models for multiple sclerosis

Dongxu Zhai[1], Shuxin Yan[1], James Samsom[1], Le Wang[1], Ping Su[1], Anlong Jiang[1], Haorui Zhang[2], Zhengping Jia[2], Izhar Wallach[3], Abraham Heifets[3], Chiara Zanato[4], Chih-Chung Tseng[4], Albert H.C. Wong[1,5,6,7], Iain R. Greig[4], Fang Liu[1,5,7,8]*

While most research and treatments for multiple sclerosis (MS) focus on autoimmune reactions causing demyelination, it is possible that neurodegeneration precedes the autoimmune response. Hence, glutamate receptor antagonists preventing excitotoxicity showed promise in MS animal models, though blocking glutamate signaling prevents critical neuronal functions. This study reports the discovery of a small molecule that prevents AMPA-mediated excitotoxicity by targeting an allosteric binding site. A machine learning approach was used to screen for small molecules targeting the AMPA receptor GluA2 subunit. The lead candidate has potent effects in restoring neurological function and myelination while reducing the immune response in experimental autoimmune encephalitis and cuprizone MS mouse models without affecting basal neurotransmission or learning and memory. These findings facilitate development of a treatment for MS with a different mechanism of action than current immune modulatory drugs and avoids important off-target effects of glutamate receptor antagonists. This class of MS therapeutics could be useful as an alternative or complementary treatment to existing therapies.

INTRODUCTION

First named as *sclérose en plaques disséminées* by the famous neurologist J.-M. Charcot in 1866, multiple sclerosis (MS) is a prototypical demyelinating disorder (*1*). Myelin is a major component of the sheath around axons, providing electrical insulation that accelerates signal conduction throughout the central and peripheral nervous system (*2*). This widespread distribution results in the myriad and variable clinical neurological deficits that occur when myelin is damaged. Clinical symptoms of MS include blindness, weakness or paralysis, heat intolerance, paresthesia, incontinence, depression, and problems with coordination and cognition (*3*). These symptoms can occur in combination and can fluctuate or persist, leading to categorization into a number of clinical subtypes: clinically isolated symptoms, relapsing-remitting MS (RRMS), primary progressive MS, and secondary progressive MS.

MS has traditionally been considered an autoimmune disorder in which $CD4^+$ T cells target myelin, leading to inflammation that causes demyelination and white matter lesions throughout the nervous system. MS has a higher prevalence in colder climates and at more northern latitudes, and this geographic distribution suggests an environmental factor (*4*). Early observations about the disease pointed to an infectious cause, such as the absence of MS in the Faroe islands north of Scotland until the arrival of British soldiers in World War II (*5*). Epstein-Barr and the Human herpesvirus-6 (HHV-6) viruses have the strongest evidence linking them to MS (*6*, *7*). Further evidence for an infectious cause or trigger is that MS can occur in geographic clusters and that people moving from low- to high-risk areas are especially vulnerable (*8*). Regardless of the initiating event, autoimmune inflammation destroys the myelin sheath in RRMS, with microglial activation and macrophages leading to neurodegeneration in progressive MS (*9*). The heritability of MS has been estimated to be 50% (*10*), and large-scale genome-wide association studies have identified many genetic variants in noncoding regions of immune system genes that are also associated with other autoimmune disorders (*11*). These variants account for approximately half of the heritability of MS (*12*).

With autoimmunity as the presumed pathophysiology of MS, the development of treatments for MS have focused on modulating the immune system. Acute episodes in RRMS are treated with a number of drugs including glucocorticoids and interferons beta 1a and 1b that increase anti-inflammatory cytokines, reduce proinflammatory cytokines, and reduce T cell activation (*13*). Glatiramer acetate resembles myelin basic protein and may thus act as a decoy to reduce T cell activation against myelin while also altering the differentiation of T cells to less inflammatory subtypes (*14*). Other immune-modulating drugs for RRMS are the monoclonal antibodies natalizumab and mitoxantrone; the anti-CD20 drugs rituximab, ocrelizumab, and ofatumumab; and the S1P inhibitor fingolimod (*15*). In contrast, there is a lack of available treatment for the progressive forms of MS, which is characterized by chronic inflammation and neurodegeneration (*16*).

An alternative pathophysiological hypothesis is that MS is primarily or initially a neurodegenerative disorder, in which the death of neurons releases myelin that in turn triggers a secondary

[1]Campbell Family Mental Health Research Institute, Centre for Addiction and Mental Health, 250 College St., Toronto M5T 1R8, Canada. [2]Department of Neurosciences & Mental Health, The Hospital for Sick Children, 686 Bay St., Toronto M5G 0A4, Canada. [3]Atomwise Inc., 221 Main Street, Suite 1350, San Francisco, CA 94105, USA. [4]Institute of Medical Sciences, University of Aberdeen, Foresterhill, Aberdeen AB25 2ZD, Scotland, UK. [5]Institutes of Medical Science, University of Toronto, 1 King's College Cir., Toronto M5S 1A8, Canada. [6]Department of Pharmacology and Toxicology, University of Toronto, 1 King's College Cir., Toronto M5S 1A8, Canada. [7]Department of Psychiatry, University of Toronto, 250 College St., Toronto M5T 1R8, Canada. [8]Department of Physiology, University of Toronto, 1 King's College Cir., Toronto M5T 1R8, Canada.
*Corresponding author. Email: fang.liu@camh.ca

autoimmune reaction (*17*). Neuroprotective strategies could thus act upstream of the autoimmune mechanisms leading to demyelination. Regardless of which model is correct, neuroprotective treatments could be effective against neurodegeneration in progressive MS and reduce autoimmunity by decreasing the myelin released by dying neurons. With this strategy in mind, targeting the processes that lead to neuronal death becomes a promising prospect for developing treatments. In particular, neuroprotection against glutamate excitotoxicity is a potential avenue that could yield effective therapies.

There is mounting evidence for the role of glutamate-mediated excitotoxicity in MS. Excess glutamate has been measured in the brains and cerebrospinal fluid of patients with MS (*18*, *19*), along with up-regulation of AMPA [2-amino-3-(3-hydroxy-5-methyl-isoxazol-4-yl) propanoic acid], NMDA (*N*-methyl-D-aspartate), and kainate ionotropic glutamate receptors (*20*). Both AMPA and NMDA inhibitors rescued neurological deficits and reduced inflammatory cytokines in the experimental autoimmune encephalitis (EAE) rodent model for MS (*21*, *22*). Our group previously found that protein interactions involving the GluA2 subunit of AMPA receptors were involved in regulating excitotoxic cell death (*23*), and disrupting these interactions reduced neurological deficits, demyelination, and axon damage in EAE mice (*24*).

Clearly, the evidence points to ionotropic glutamate receptors as a target for neuroprotection in MS. Inhibitors of AMPA and NMDA receptors have problematic side effect profiles due to the ubiquity of these receptors in the central nervous system (CNS) and their critical role in brain function (*25*, *26*). Fortuitously, the structure of AMPA receptors is well characterized (*27*), allowing for detailed molecular simulation of binding sites for potential allosteric modulators of AMPA function, which may provide neuroprotection while limiting potential off-target effects. We previously identified a binding site outside of the canonical ligand-binding domain within the GluA2 AMPA subunit (*23*). We hypothesize that this site is critical for regulating AMPA-mediated excitotoxicity and could serve as a potential target for small-molecule treatments for MS.

To advance the development of a viable treatment for MS that provides neuroprotection by targeting glutamate excitotoxicity, we identified a number of drug-like small-molecule candidates that were predicted to bind to our discovered allosteric site using a convolutional neural network approach to screen a large chemical space (*28*). Here, we report the results of experiments to test the efficacy of these small molecules in restoring neurological function and myelination in the mouse models for MS. These data are a proof of principle that a small-molecule allosteric modulator affecting AMPA-mediated excitotoxicity could have potential as a treatment for MS.

RESULTS

In silico screen identifies small molecules likely to bind the GluA2 allosteric binding site

We used an artificial intelligence–enabled approach to predict small-molecule binding to the GluA2 AMPA subunit. We had previously identified a 30–amino acid fragment in the N-terminal region of GluA2 (Y142 to K172), which we found was critical for regulating the role of AMPA in excitotoxic cell death (*23*). This region was used as the target binding site for the AtomNet deep neural network, which had previously been trained on a general set of thousands of proteins and millions of ligands.

Our discovered allosteric binding site was specified as the target for our in silico screen using the 3KG2 structure of GluA2 downloaded from the Protein Data Bank (PDB) (Fig. 1). The chemical space screened started with the 8.2 million molecules in the ZINC catalog, which was narrowed down to 1.2 million by our criteria to filter out compounds with problematic properties, e.g., salts, autofluorescers, redox cyclers, duplicates, and compounds unlikely to cross the blood-brain barrier. The remaining compounds were algorithmically clustered on the basis of scaffold, and exemplar compounds from each cluster were chosen to ensure diversity of compound coverage. Unlike a focused library for well-studied targets such as kinases, we had no a priori reason to constrain the screened compounds toward certain chemotypes. All the remaining 523,140 molecules were rank-ordered by AtomNet score. Last,

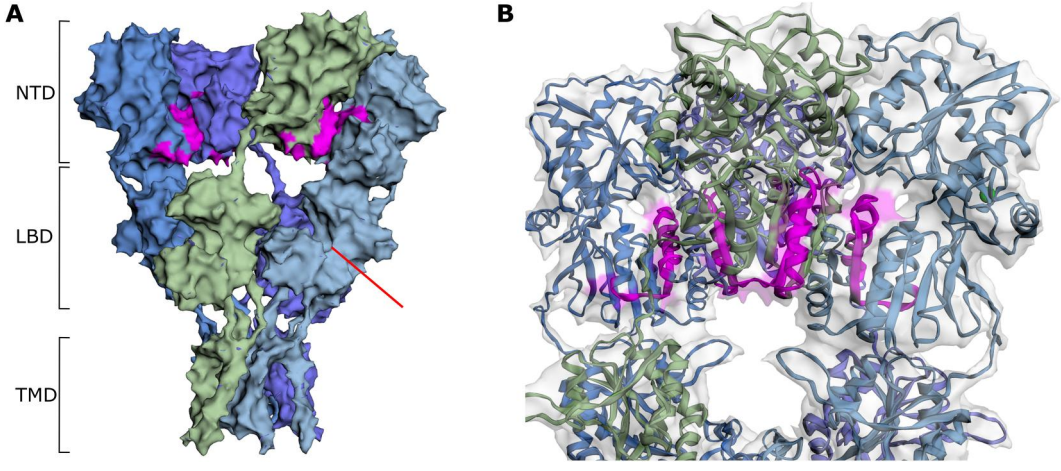

Fig. 1. Illustration of the binding site on the AMPA glutamate receptor 2 (GluA2) structure used for the virtual screening. (**A**) GluA2 x-ray crystal structure downloaded from the PDB (ID: 3KG2) showing the N-terminal domain (NTD), ligand-binding domain (LBD), and transmembrane domain (TMD). The allosteric binding site used as the target for screening is marked in magenta. The orthosteric active site within the LBD cleft forming the binding pocket for agonist and competitive antagonist drugs is indicated with a red arrow. (**B**) Enlarged view of the screening target binding site. Structures were rendered using EzMol.

compounds that cost over $200 were eliminated, and the top 50 molecules were bought for further characterization. At no point were compounds manually cherry-picked.

Screening and refinement of candidates to select pharmacologically suitable lead compounds

The 50 candidates identified in our in silico screen were tested for the ability to block glutamate-mediated excitotoxicity in human embryonic kidney (HEK) 293 cells stably expressing GluA1 and GluA2. Potency of molecules of interest in preventing cell death was acquired from concentration curves. Three promising hits were identified, each based on the unusual pyrrolo-pyrazole skeleton. These showed good potency [median inhibitory concentration (IC_{50}) < 300 nM] and, in the case of compound **1** (YH668), moderate in vitro stability (human and rat liver microsomes $T_{1/2}$ = 73 and 37 min, respectively). Compound **1** was selected for optimization.

As shown in Fig. 2A, a range of left-hand side aryl/heteroaryl rings were tolerated (compound **2**: W, X, Y, and Z = CH or N), most favorably bearing an electron-withdrawing group at the meta-position as shown. The right-hand benzyl group was moved to the other pyrrole nitrogen, resulting in slightly more potent but much more metabolically stable analogs (compounds **3** to **5**). A comparison of representative positional isomers (compounds **1** and **3)** showed an improvement in potency from 200 to 35 nM and an increase in rat and human liver microsomal half-lives from 37 to 309 min and from 73 to 329 min, respectively. There was a flat structure-activity relationship (SAR), punctuated by unexplained activity cliffs: A wide range of modifications to the R_3 substituents at the right-hand side of compound **2** were tolerated with no loss of potency; however, some closely related modifications could lead to a dramatic loss of potency (see the Supplementary Materials). The SAR associated with these modifications was in turn affected by the nature of the left-hand aromatic/heteroaromatic ring, and no simple relationship could be determined. Studies indicated that the carboxamide shown in compounds **1** to **5** was optimal for potency but that a wide range of cyclic and acyclic secondary or tertiary amides were tolerated (R_1 and R_2 substituents in compound **2**). On the other hand, the structure property relationship was extremely brittle, and small changes in structure could have dramatic effects on solubility, stability, permeability, or efflux. Thus, only a small number of compounds had suitable in vitro ADME (absorption, distribution, metabolism, and excretion) properties.

In vitro models indicated that compound **3** (pyrazine: X = N, Y = CH, and Z = N), compound **4** (pyrimidine: X = CH, Y = N, and Z = N), and compound **5** (phenyl: X = CH, Y = CH, Z = CH) had low risks for cardiotoxicity (hERG), cytotoxicity (HepG2), mutagenicity (Ames), and CYP450 inhibition (five common isoforms) with a ~1000-fold window between the IC_{50} for each and IC_{50} versus our target. Furthermore, compound **3** did not hit any targets in the SafetyScreen44 assay at 10 μM (ligand displacement <50% at all targets, with the exception of D_2 at 54%). These compounds were confirmed for potency to inhibit glutamate-mediated toxicity (Fig. 2, B to D, and table S1).

These compounds all had good oral bioavailability (e.g., ZCAN155: 58%; ZCAN262: 90%) and, as shown in Fig. 2E, acceptable plasma protein and brain tissue binding. Contrary to the high in vitro stability in liver microsomes and hepatocytes, the in vivo half-life was measured at only around 1 hour, presumably due to the low volume of distribution (V_d). Other non-CYP450–mediated routes of metabolism (aldehyde oxidase and xanthine oxidase) were not found to be involved. A number of attempts were made to increase the logP to increase V_d (and reduce renal clearance, should it be an additional factor), but these proved of limited benefit and were associated with increased metabolic clearance and, thus, no improvement in half-life.

The addition of a second fluorine to compound **4** (compound **6**—ZCAN262) gave apparent incremental improvements in each of human, rat, and mouse microsomal stability, and this compound was selected for further in vivo characterization. As predicted, the small increase in vitro in mouse (105 versus 141 min) did not lead to any enhancement of in vivo half-life; however, the larger improvement seen in rat liver microsomes (an increase from 158 to 451 min) prompted further investigation in a rat model and, although the V_d remained low, there was a considerable reduction in clearance (<5 ml min^{-1} kg^{-1}; <10% liver blood flow), which proved sufficient to give a brain half-life of >2.5 hours (2.6 and 4.2 hours in separate experiments). Crucially, ZCAN262 had a marked improvement in CNS exposure and allowed for $C_{min\ unbound}$ to remain above the IC_{50} versus the target (estimated free concentration 128 nM at 24 hours following a 10-mg/kg dose). Thus, ZCAN262 was selected as our top preclinical candidate compound in the treatment of MS, which binds our discovered allosteric site.

All three candidate molecules improve neurological function in EAE mice

We further evaluated the effect of compounds **1** (YH668), **3** (ZCAN155), and **6** (ZCAN262) on neurological function in vivo using the EAE model, which is the most common autoimmune mouse model for MS. The parent YH668 significantly improved clinical scores ($F_{1,10}$ = 120.9, P < 0.00001, η_p^2 = 0.92 [0.81; 1]) (Fig. 3A). Post hoc marginal means comparisons showed significant improvements starting almost immediately from day 13 after induction all the way to day 28, but there was no interaction with time ($F_{17,159}$ = 1.14, P = 0.32, η_p^2 = 0.11 [0; 1]). The mean effect size for reduction in clinical score across pairwise comparisons for significant time points was d = −2.13 [−3.36; −0.91]. ZCAN155 was, likewise, able to improve EAE clinical scores in a dose-dependent manner ($F_{2,22}$ = 26.6, P < 0.00001, η_p^2 = 0.71 [0.50; 1]) with a significant interaction over time ($F_{38,407}$ = 2.71, P < 0.00001, η_p^2 = 0.20 [0.08; 1]) (Fig. 3B). Improvements crossed the significance threshold starting from day 15, and the mean effect size for significant reductions in clinical scores was d = −2.21 [−3.55; −0.88] at 5 mg/kg and d = −3.45 [−4.79; −2.11] at 10 mg/kg. The most potent of our molecules was ZCAN262, which caused significant reductions in EAE scores ($F_{2,23}$ = 95.9, P < 0.00001, η_p^2 = 0.89 [0.81; 1]) with a significant interaction over time ($F_{30,358}$ = 2.20, P = 0.00042, η_p^2 = 0.16 [0.04; 1]) (Fig. 3C). Reductions became significant starting from day 13, and the mean effect size for significant reductions was d = −1.69 [−2.68; −0.70] at 2.5 mg/kg and d = −2.08 [−3.07; −1.09] at 5 mg/kg. Hence, ZCAN262 showed comparable effects to YH668 at a lower dose. ZCAN155 had large pairwise effects, but they became significant at later time points than either YH668 or ZCAN262, and the overall effect size was smaller. Nevertheless, all three compounds improved motor function in EAE mice.

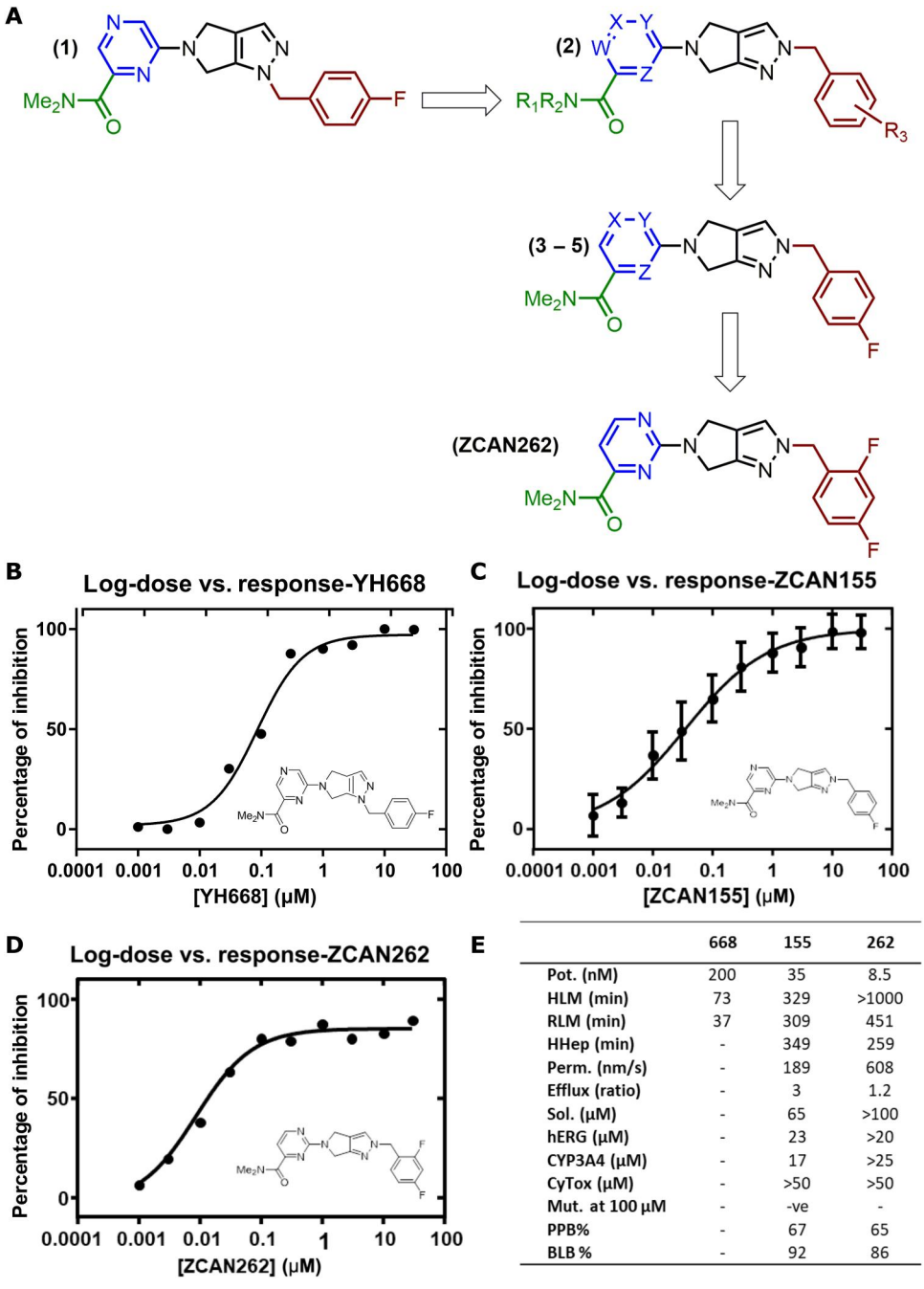

E

	668	155	262
Pot. (nM)	200	35	8.5
HLM (min)	73	329	>1000
RLM (min)	37	309	451
HHep (min)	-	349	259
Perm. (nm/s)	-	189	608
Efflux (ratio)	-	3	1.2
Sol. (μM)	-	65	>100
hERG (μM)	-	23	>20
CYP3A4 (μM)	-	17	>25
CyTox (μM)	-	>50	>50
Mut. at 100 μM	-	-ve	-
PPB%	-	67	65
BLB %	-	92	86

Fig. 2. Structures of compound 1 (YH668), compound 3 (ZCAN155), and compound 6 (ZCAN262). (**A**) Dose response of glutamate-induced cell death to different concentrations of YH668 (**B**), ZCAN155 (**C**), and ZCAN262 (**D**). (**E**) Summary of in vitro ADMET for YH668, ZCAN155, and ZCAN262. Pot, potency in cell death model; HLM/RLM, half-life in human/rat/mouse liver microsomal stability assays, respectively; HHep, half-life in human hepatocyte stability assay; Perm, Papp A-B in MDR1-MDCK permeability assay; Efflux, Papp B-A/A-B in MDR1-MDCK permeability assay; Sol, kinetic solubility in water; hERG, IC_{50} for inhibition of hERG channel; CYP3A4, IC_{50} for inhibition of CYP3A4 function; Mut at 100 μM, presence or absence of mutagenic effect in Ames assay at 100 μM; PPB%, % plasma protein binding; BLB, % brain lipid/tissue binding.

ZCAN262 improves neurological function in the cuprizone-diet MS mouse model

No single animal model captures all the features of MS, with the main and obvious shortcoming being in construct validity: No mouse spontaneously develops MS, so an artificial inducer is required. Since the etiology of MS remains uncertain, we chose to supplement our data from the autoimmunity-based EAE model with a neurotoxin model; cuprizone is the most widely used toxin model for MS. We also expanded the range of neurological tests to include open field locomotion (Fig. 3, D and E) and the rotarod (Fig. 3, F and G). Treatment significantly affected distance traveled ($F_{2,28}$ = 5.69, P = 0.0084, η^2 = 0.29 [0.06; 1]) and velocity ($F_{2,28}$ =

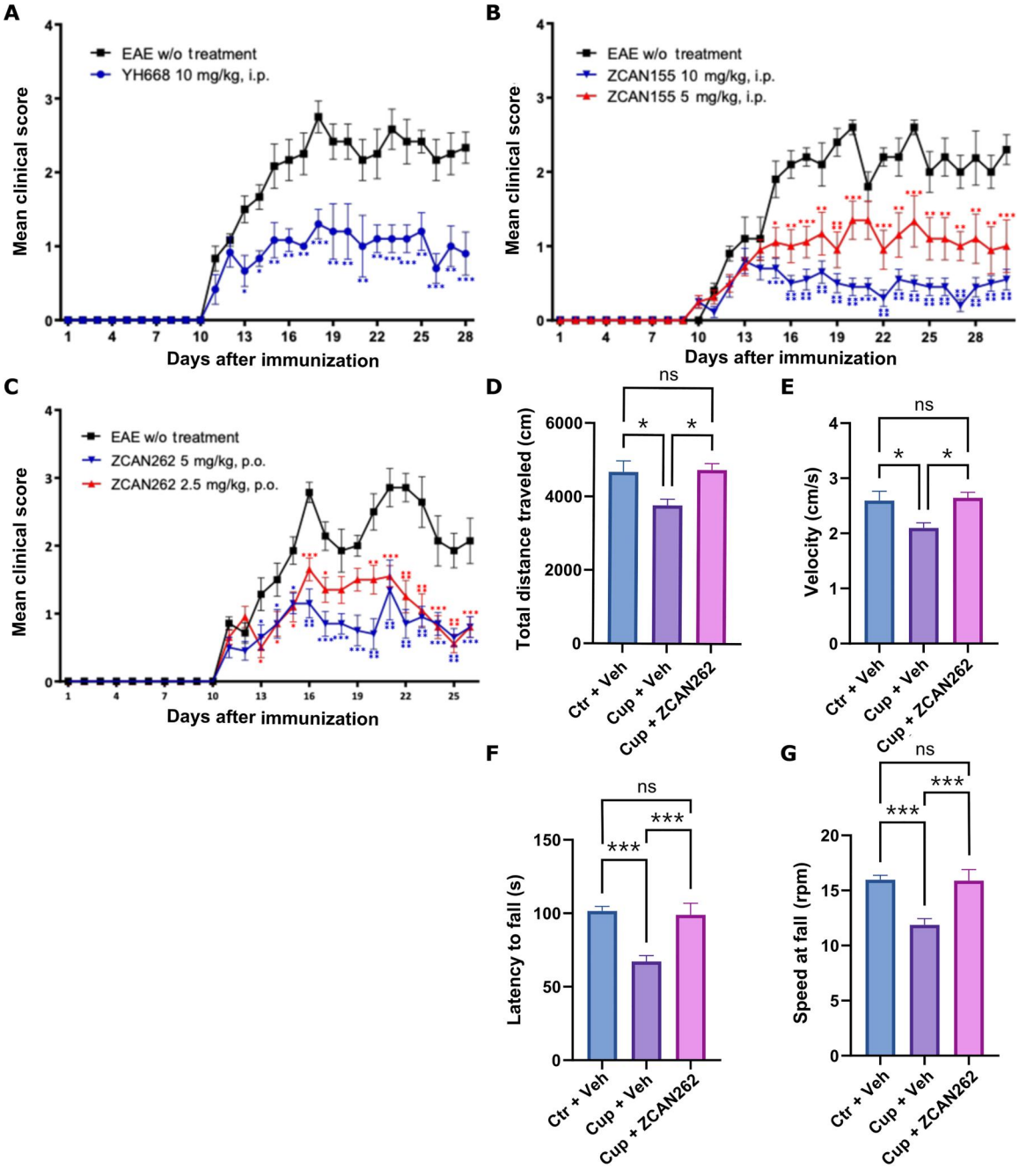

Fig. 3. Treatment with our novel compounds significantly improves motor function in the EAE and cuprizone-diet models for MS. EAE clinical scoring treated daily with YH668 (**A**), ZCAN155 (**B**), and ZCAN262 (**C**) using intraperitoneal (i.p.) or oral administration (ZCAN262) starting after clinical symptoms begin to occur (day 11 after immunization) in the EAE mouse model for MS. Repeated-measures analysis of variance (ANOVA) (YH668 $n = 6$, EAE $n = 6$; ZCAN155 $n = 10$ each dose, EAE $n = 5$; ZCAN262 $n = 10$ each dose, EAE $n = 7$), post hoc marginal means. Distance traveled over a 90-min period (**D**) and mean velocity (**E**) in the open field test in control-diet (Ctr) + oral vehicle (Veh), cuprizone-diet (Cup) + Veh, and Cup + oral ZCAN262–treated mice. Latency to fall (**F**) and the speed at which mice fell (**G**) from the rotarod. Oral treatments started after 2 weeks on the cuprizone diet. ANOVA with post hoc Tukey's HSD, $n = 10$ per group. Error bars represent means ± SEM; ns, not significant; $^{*}P < 0.05$, $^{**}P < 0.01$, $^{***}P < 0.001$, $^{****}P < 0.0001$.

5.66, $P = 0.0086$, $\eta^2 = 0.29$ [0.05; 1]) in the open field. Post hoc comparisons showed that ZCAN262 restored both locomotor activity (control versus saline $P = 0.020$, $d = 1.20$ [0.29; 2.12]; saline versus ZCAN262 $P = 0.022$, $d = -1.29$ [−2.29; −0.29]; control versus ZCAN262 $P = 0.98$, $d = -0.09$ [−1.04; 0.86]) and mean velocity (control versus saline $P = 0.022$, $d = 1.19$; saline versus ZCAN262 $P = 0.021$, $d = -1.30$ [−2.31; −0.30]; control versus ZCAN262 $P = 0.97$, $d = -0.12$ [−1.07; 0.84]) to levels indistinguishable from control-diet mice when compared with saline-treated mice. Likewise, treatment significantly improved both time to fall ($F_{2,28} = 13.15$, $P < 0.00001$, $\eta^2 = 0.48$ [0.24, 1]) and rotational velocity at fall ($F_{2,28} = 65.45$, $P < 0.00001$, $\eta^2 = 0.49$ [0.24, 1]) in the rotarod test. ZCAN262 restored both falling latency (control versus saline $P = 0.0003$, $d = 2.00$ [0.95; 3.04]; saline versus ZCAN262 $P = 0.0006$, $d = -1.85$ [−2.88; −0.82]; control versus ZCAN262 $P = 0.94$, $d = 0.15$ [−0.77; 1.06]) and falling rpm (control versus saline $P = 0.0004$, $d = 1.93$ [0.89; 2.97]; saline versus ZCAN262 $P = 0.0003$, $d = -1.95$ [−2.99; −0.91]; control versus 262 $P = 0.99$, $d = -0.023$ [−0.94; 0.89]) to control-diet mice levels relative to saline-treated cuprizone-diet mice. This shows that ZCAN262 caused dramatic improvement in measures of neurological dysfunction in the cuprizone-diet demyelination model for MS.

ZCAN262 restores myelination, axon integrity, and oligodendrocytes in the cuprizone-diet mouse model for MS

In conjunction with the rescue of neurological function by ZCAN262 in the cuprizone mouse in vivo, we analyzed the histopathology effects of this drug postmortem. We focused on a subset of immunohistochemical and electron microscopic analyses relevant to the core pathology of MS: myelin, axon number and integrity, myelin thickness on axons, oligodendrocyte numbers, and activated microglial infiltration. The corpus callosum contains heavily myelinated axons that form a major white matter tract connecting the cerebral hemispheres and is an easily demarcated structure for histological analysis of myelination.

Figure 4 (A to C) clearly shows the almost complete rescue of myelin with ZCAN262 treatment in the corpus callosum to that of control mice without cuprizone treatment. Daily treatments significantly affected FluoroMyelin intensity in both the medial ($F_{2,54} = 16.12$, $P < 0.00001$, $\eta^2 = 0.37$ [0.20;1]) and lateral ($F_{2,118} = 25.86$, $P < 0.00001$, $\eta^2 = 0.30$ [0.19; 1]) corpus callosum. There was significant demyelination in cuprizone-fed mice compared to controls (medial $P < 0.00001$, $d = 1.74$ [1.03; 2.45]; lateral $P < 0.00001$, $d = 1.47$ [1.00; 1.93]). Post hoc Tukey's revealed significant improvements in FluoroMyelin intensity between treated and untreated cuprizone-fed mice (medial $P = 0.0018$, $d = 1.22$ [0.50; 1.93]; lateral $P < 0.00001$, $d = 1.15$ [0.67; 1.64]), with levels in treated restored to that of the control-diet–fed mice (medial $P = 0.26$, $d = 0.52$ [−0.15; 1.20]; lateral $P = 0.37$, $d = 0.31$ [−0.15; 0.77]).

A more detailed electron microscope examination of axon structure is illustrated with sample images in Fig. 5A. We quantified myelinated axon number, myelin thickness, and the g ratio (the inner-to-outer diameter of the myelin sheath) as metrics for axonal integrity (*29*). ZCAN262 treatment significantly affected myelinated axon density ($F_{2,142} = 43.97$, $P < 0.00001$, $\eta^2 = 0.42$ [0.31; 1]) (Fig. 5B), myelin thickness ($F_{2,362} = 69.04$, $P < 0.00001$, $\eta^2 = 0.28$ [0.21; 1]) (Fig. 5C), and myelin g ratio ($F_{2,362} = 75.36$, $P < 0.00001$, $\eta^2 = 0.29$ [0.23; 1]) (Fig. 5, D and E). Post hoc Tukey's showed that cuprizone diet significantly affected all three measures of myelin integrity (density: $P < 0.00001$, $d = 1.72$ [1.24; 2.19]; thickness: $P < 0.00001$, $d = 1.37$ [1.10; 1.65]; g ratio: $P < 0.00001$, $d = -1.36$ [−1.64; −1.09]). ZCAN262 significantly improved these measures (density: $P < 0.00001$, $d = 1.81$ [1.32; 2.30]; thickness: $P < 0.00001$, $d = 1.20$ [0.93; 1.46]; g ratio: $P < 0.00001$, $d = -1.33$ [−1.59; −1.06]), with treated mice restored to levels indistinguishable from control-diet–fed mice (density: $P = 0.91$, $d = -0.09$ [−0.53; 0.34]; thickness: $P = 0.36$, $d = 0.18$ [−0.08; 0.44]; g ratio: $P = 0.96$, $d = -0.036$ [−0.29; 0.22]). To control for the effects of axon diameter on measurements, a fixed-slopes general linear model was fitted. There was a significant relationship between axon diameter and myelin thickness ($t = 16.0$, $P < 0.00001$, Std. Coef. = 0.55 [0.48; 0.61]). Cuprizone diet significantly shifted this relationship ($t = 12.5$, $P < 0.00001$, Std. Coef. = 0.10 [−0.06; 0.27]), while ZCAN262 and vehicle treatments did not differ ($t = 1.22$, $P = 0.23$, Std. Coef. = 0.55 [0.48; 0.61]). These data show that ZCAN262 completely restores myelin to the normal levels seen in mice not treated with cuprizone.

Significant, though less dramatic effects are seen with ZCAN262 treatment on restoring oligodendrocyte counts in the cuprizone mouse corpus callosum, as visualized by olig2 antibody staining ($F_{2,68} = 230.3$, $P < 0.00001$, $\eta^2 = 0.87$ [0.83; 1]) (Fig. 6, A to C). Cuprizone diet significantly reduced olig2$^+$ cell number ($P < 0.00001$, $d = 5.60$ [4.48; 6.71]). While treatment increased cell number relative to vehicle ($P = 0.013$, $d = 0.89$ [0.26; 1.52]), counts were still significantly reduced relative to control-diet–fed mice ($P < 0.00001$, $d = 4.71$ [3.72; 5.70]).

We also observed a reduction in the number of corpus callosum Iba$^+$ cells as a result of ZCAN262 treatment, though not to that of non–cuprizone-treated control mice ($F_{2,139} = 306.1$, $P < 0.00001$, $\eta^2 = 0.81$ [0.77; 1]) (Fig. 7, A and B). Cuprizone diet significantly increased Iba$^+$ cell number ($P < 0.00001$, $d = -5.03$ [−5.76; −4.31]), indicative of an inflammatory response. Treatment reduced cell number relative to vehicle ($P < 0.00001$, $d = -2.16$ [−2.66; −1.67]), but counts were still significantly elevated relative to control-diet–fed mice ($P < 0.00001$, $d = -2.87$ [−3.39; −2.35]).

Last, we examined markers of neuronal infiltration and axonal damage using NeuN and Neurofilament-H staining as these are important processes in MS pathology. As shown in figs. S1 and S2, ZCAN262 treatment had no effect on NeuN$^+$ cell number or Neurofilament-H green intensity.

Together, we show that ZCAN262 was able to completely restore myelin integrity in the cuprizone-diet model of demyelination in MS. There were also positive effects on oligodendrocyte proliferation and one measure of neuroinflammation. However, the treatment did not improve measures of neuron infiltration into the corpus callosum or axon integrity.

ZCAN262 has no effect on glutamate-mediated basal neurotransmission and recognition memory or spatial learning

Clinical use of glutamate receptor modulators is limited by the critical role of glutamate receptors in excitatory neurotransmission (*25*). Thus, our promising results showing that ZCAN262 can improve neurological function and protect myelin, oligodendrocytes, and axons would not be clinically useful if ZCAN262 blocks AMPA receptor–mediated neurotransmission. Thus, we

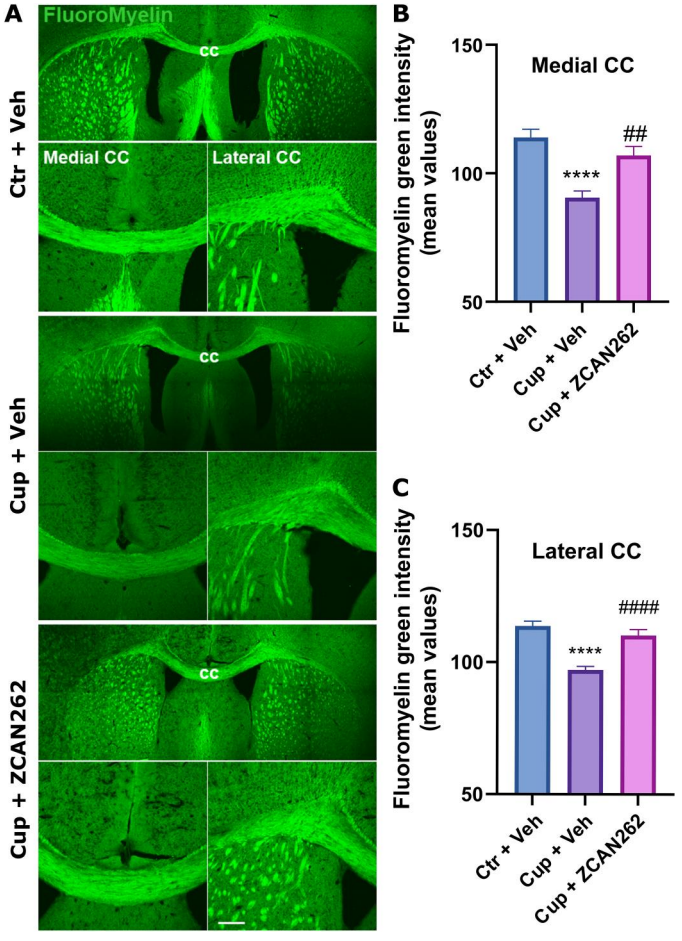

Fig. 4. Administration of ZCAN262 rescued demyelination in cuprizone-diet mice measured with FluoroMyelin staining. (**A**) Representative confocal images of FluoroMyelin Green staining in control-diet (Ctr) + oral vehicle (Veh), cuprizone-diet (Cup) + Veh, and Cup + oral ZCAN262–treated mouse brain slices. The lower panels show the medial corpus callosum (CC) and lateral CC. Scale bar, 200 μm. CC: corpus callosum. (**B**) Quantification of the mean FluoroMyelin intensity in the medial CC (n = 16 to 21 views from three mice per group). (**C**) Quantification mean FluoroMyelin intensity in the lateral CC (n = 32 to 45 views from three mice per group). Error bars represent means ± SEM, one-way ANOVA, post hoc Tukey's, ****P < 0.0001 compared to Ctr + Veh, ##P < 0.01 compared to Cup + Veh, ####P < 0.0001 compared to Cup + Veh.

conducted electrophysiological recordings in hippocampal Schaffer collaterals to examine the effects of ZCAN262 on basal synaptic transmission and paired-pulse facilitation (PPF).

As expected, there was a significant effect of stimulus intensity on field excitatory postsynaptic potential (fEPSP) peak amplitude ($F_{4,120}$ = 157.2, P < 0.0001, η_G^2 = 0.59). There was no effect of treatment ($F_{1,30}$ = 0.011, P = 0.92, η_G^2 = 0.0003) or interaction between treatment and stimulus ($F_{4,120}$ = 0.50, P = 0.073, η_G^2 = 0.0045) on fEPSP amplitude (Fig. 8A). To compare input/output between treatments, a general linear mixed effect model was fitted (marginal R^2/conditional R^2 = 0.56/0.80). There is a significant positive relationship between fEPSP amplitude and fiber volley amplitude (t_{153} = 4.65, P < 0.0001, β = 1.66, Std. Coeff. = 0.45 [0.26; 0.64]) as well as stimulus intensity (t_{153} = 3.20, P = 0.0017, β = 0.21, Std. Coeff. = 0.29 [0.11; 0.47]) (Fig. 8B). There was no effect of treatment (t_{47} = −0.14, P = 0.89, β = −0.028, Std. Coeff. = 0.12 [−0.26; 0.50]) or interaction between treatment and fiber volley (t_{132} = 1.43, P = 0.15, β = 0.44, Std. Coeff. = 0.12 [−0.05; 0.28]). Fiber volley amplitude and stimulus intensity were highly multicollinear, so the true effects of these could not be estimated in this model. If a model is fitted without controlling for stimulus intensity (marginal R^2/conditional R^2 = 0.56/0.80), the interaction between treatment and fiber volley amplitude becomes significant (t_{131} = 2.24, P = 0.026, β = 0.69, Std. Coeff. = 0.19 [0.02; 0.35]). The estimated slope of the relationship between fEPSP and fiber volley amplitude was slightly higher in ZCAN262 (β = 3.30)− than vehicle (β = 2.60)−treated animals. This suggests that ZCAN262 treatment may enhance basal synaptic transmission in hippocampal circuits in a stimulus-dependent manner, although the relationship is weak and disappears when stimulus intensity is controlled for. Overall, and accounting for stimulus intensity, there was no evidence that ZCAN262 treatment altered basal synaptic transmission.

PPF is a type of short-term synaptic plasticity that arises from presynaptic signaling mechanisms affecting vesicle release (*30*). There was a significant effect of stimulus interval on paired-pulse ratio ($F_{7,210}$ = 172.2, P < 0.0001, η_G^2 = 0.60), showing that there was effective PPF (fig. S3C). There was no main effect of ZCAN262 treatment on paired-pulse ratio ($F_{1,30}$ = 3.38, P = 0.076, η_G^2 = 0.077), but there was a significant interaction between treatment and stimulus interval ($F_{7,210}$ = 2.81 P = 0.0080, η_G^2 = 0.024). Post hoc contrasts revealed that this effect was driven by higher paired-pulse ratio in ZCAN262-treated animals at shorter stimulus intervals (25 ms, t_{54} = 2.25, P = 0.076, d = 1.46 [0.15; 2.76]; 50 ms, t_{54} = 2.83, P = 0.032, d = 1.83 [0.52; 3.14]; 100 ms, t_{54} = 2.76, P = 0.032, d = 1.79 [0.48; 3.49]). This suggests that ZCAN262 treatment may weakly potentiate presynaptic release probability at low stimulus intervals.

Compounds that disrupt synaptic transmission may affect cognition. We measured recognition memory and spatial learning in wild-type mice treated chronically with ZCAN262 to ensure that there was no disruption in common measures of learning and memory.

The novel object recognition test (NORT) was used to measure recognition memory. There was no effect of ZCAN262 treatment on how much the mice inspected the objects during familiarization (t_{16} = −0.70, P = 0.50, d = 0.34 [−1.31; 0.64]) (fig. S3A). As expected, mice spent significantly more time with the novel object during the novelty phase ($F_{1,22}$ = 9.19, P = 0.0061, η_G^2 = 0.16), averaging 24.2 s [10; 42.3] longer, demonstrating that the mice remembered the familiar object (fig. S3A). There was no effect of treatment ($F_{1,22}$ = 1.42, P = 0.25, η_G^2 = 0.035) or interaction ($F_{1,22}$ = 0.025, P = 62, η_G^2 = 0.005) on inspection time in the novelty phase. Furthermore, there was no effect of ZCAN262 treatment on discrimination index (DI) (t_{21}= 0.079, P = 0.94, d = 0.03 [−0.82; 0.89]) (fig. S4B). This suggests that ZCAN262 had no impact on recognition memory.

Spatial learning was assessed in the Morris water maze (MWM). First, there was no effect of ZCAN262 treatment on swimming velocity (t_{19} = −0.33, P = 0.74, d = −0.15 [−1.05; 0.75]) (fig. S3C). Mice took significantly less time to find the platform with each training day ($F_{3,66}$ = 12.86, P < 0.0001, η_p^2 = 0.37) showing effective learning of the platform position (fig. S3D). There was no main effect of treatment ($F_{1,22}$ = 0.0015, P = 0.97, η_p^2 < 0.0001) or interaction between treatment and training ($F_{3,66}$ = 0.83, P = 0.48, η_p^2 = 0.04). This suggests that ZCAN262 did not affect spatial learning.

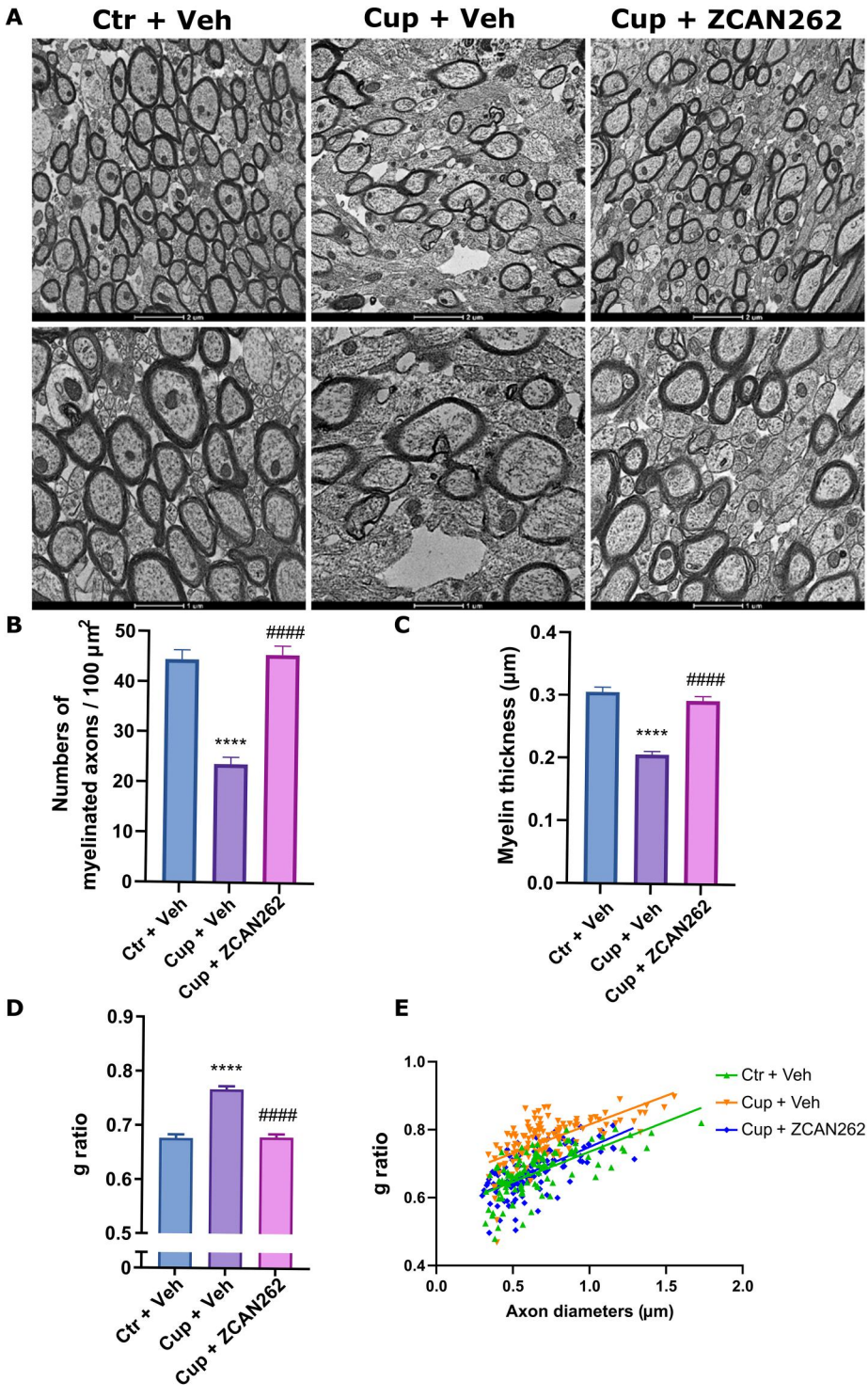

Fig. 5. Administration of ZCAN262 rescued demyelination in cuprizone-diet mice measured by electron microscopy. (**A**) Representative corpus callosum (CC) electron microscopy images in control-diet (Ctr) + oral vehicle–treated (Veh), cuprizone-diet (Cup) + Veh, and Cup + oral ZCAN262–treated mice. The lower panel images show a higher magnification. (**B**) Quantification of the density of myelinated axons per 100 μm^2. n = 39 to 62 views from three to four mice per group. (**C**) Quantification of the Myelin thickness, n = 109 to 129 axons from three to four mice each group. (**D**) Quantification of the g ratio of the myelinated axons. n = 109 to 129 axons from three to four mice each group. (**E**) The scatterplot showing the individual g-ratio values and axonal diameter distribution, fixed-slopes general linear model. Error bars represent means ± SEM, one-way ANOVA unless otherwise indicated, post hoc Tukey's, ****P < 0.0001 versus Ctr + Veh; ####P < 0.0001 versus Cup + Veh.

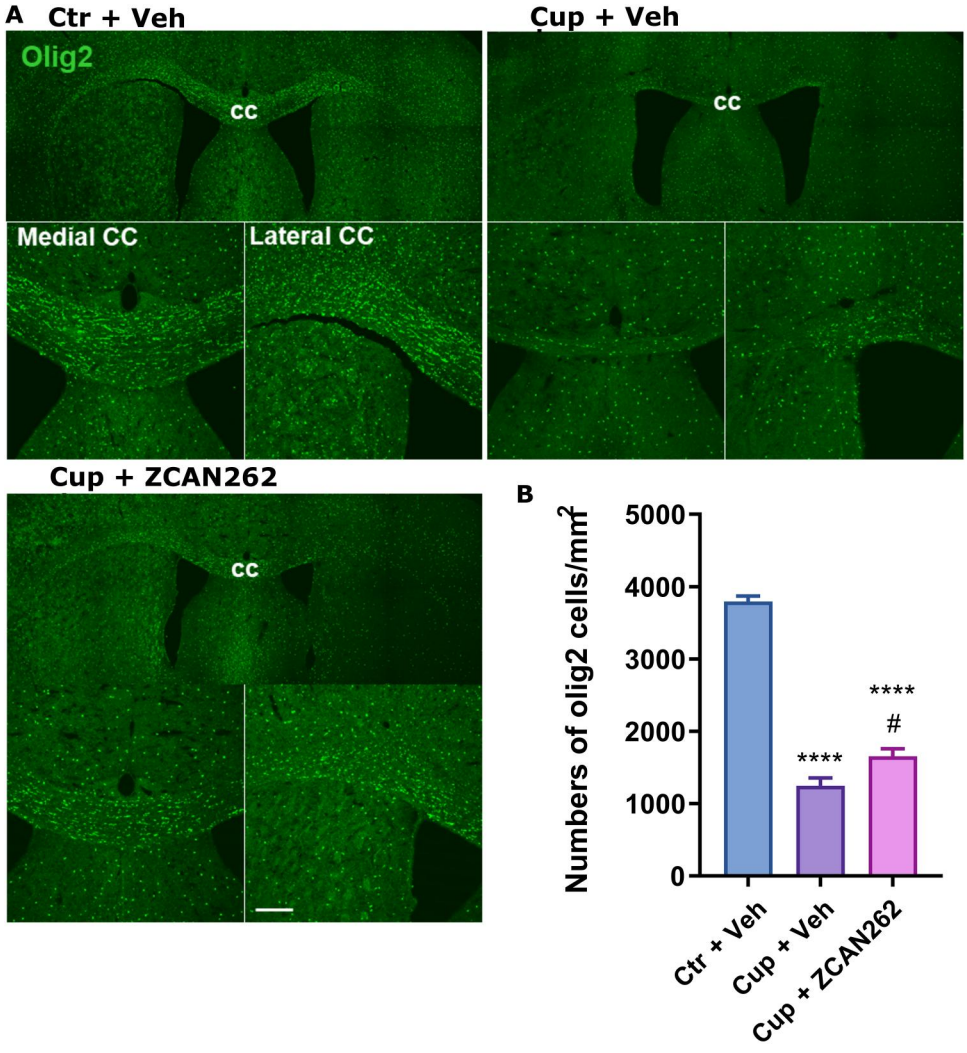

Fig. 6. Administration of ZCAN262 increased number of corpus callosum oligodendrocytes in cuprizone-diet mice. (**A**) Representative confocal images of staining with antibody against Olig2 in control-diet (Ctr) + oral vehicle (Veh), cuprizone-diet (Cup) + Veh, and Cup + oral ZCAN262–treated mouse brain slices. The lower panel images show the medial corpus callosum (CC) and lateral CC from each group. Scale bar, 200 μm. (**B**) Quantification shows the density of oligodendrocyte-lineage cells in the CC. $n = 21$ to 28 views from three mice per group, error bars represent means ± SEM, one-way ANOVA, post hoc Tukey's, ****$P < 0.0001$ compared to Ctr + Veh, #$P = 0.0131$ compared to Cup + Veh.

Together, we have evidence that ZCAN262 can improve MS pathology without disrupting basal synaptic transmission or measures of recognition memory and spatial learning. There was evidence for potentiation of short-term synaptic plasticity, but these effects did not negatively affect functional measures of cognition.

DISCUSSION

We have found a small-molecule compound that has therapeutic effects in mouse models for MS and has potential for further drug development. In summary, we used in silico methods to identify three candidate small molecules that bind to an allosteric binding site on the GluA2 AMPA subunit: YH668, ZCAN155, and ZCAN262. All three compounds produce substantial improvements in neurological deficits in EAE mice in vivo at doses between 1 and 10 mg/kg. We elected to perform additional experiments with ZCAN262, which restored open field locomotion and rotarod performance in cuprizone MS model mice to that of normal control mice. ZCAN262 also restored myelination, the number of myelinated axons, and myelin thickness in cuprizone-treated mice to healthy control levels. Less dramatic but still notable rescue to oligodendrocyte numbers was also seen in conjunction with reduction in activated microglia.

While promising, these results of course require replication and could also be extended to include additional cellular and molecular characterization of the effects on both EAE and cuprizone mouse models. In particular, it would be useful to dissect the impact of our compounds on molecular regulators of excitotoxicity, cellular markers of neurodegeneration, and myriad immunological phenotypes including T cell subtype quantification, pro- and anti-inflammatory cytokine levels, and entry of immune cells into the CNS. Additional clinical phenotyping of therapeutic effects in mouse

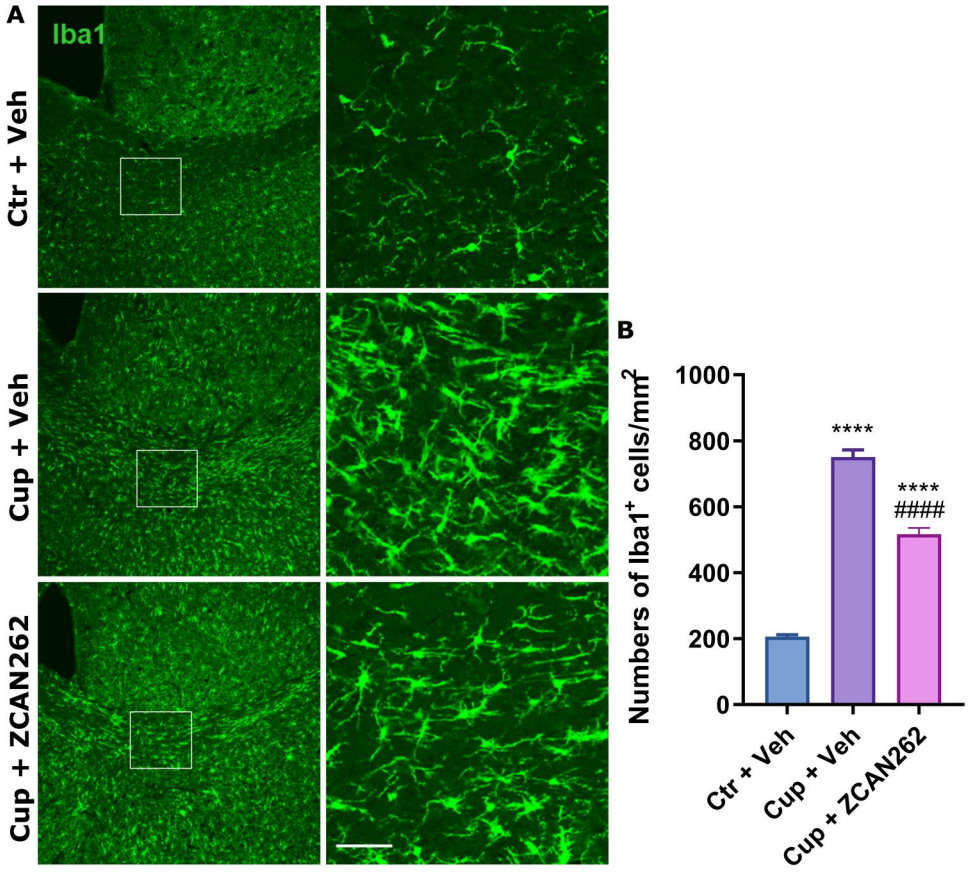

Fig. 7. Administration of ZCAN262 decreased inflammatory response in the corpus callosum of cuprizone-diet mice. (**A**) Representative confocal images of anti-Iba1 staining in control-diet (Ctr) + oral vehicle (Veh), cuprizone-diet (Cup) + Veh, and Cup + oral ZCAN262–treated mouse brain slices. White boxes indicate the region scaled up in the left image. Scale bar, 50 μM. (**B**) Quantification of the density of microglia in the corpus callosum (CC). $n = 42$ to 54 views from three mice per group, error bars represent means ± SEM, one-way ANOVA, post hoc Tukey's, ****$P < 0.0001$ compared to Ctr + Veh, ####$P < 0.0001$ compared to Cup + Veh.

models, including nerve conduction and live in vivo imaging, would provide further support for the viability of these compounds as potential drug treatments for MS in humans.

There are many existing immune-modulating drugs used to treat RRMS, but our potential drug candidates exploit a different therapeutic strategy: neuroprotection. It is possible that one of our compounds could be used in conjunction with current immunological treatments and could have complementary effects. As with cancer chemotherapy drug cocktails, simultaneous targeting of a disease pathway at multiple points can have synergistic effects that result in better outcomes and fewer side effects than monotherapy. Another potential application of our small-molecule compounds could be to treat the progressive forms of MS, for which there are no effective treatments available to arrest the neurodegeneration and accumulating neurological deficits.

An important limitation of this paper is the reliance on mouse models, which can only capture some aspects of MS in humans. Cross-species translation is imperfect, since both animal models consist of initiating inflammatory demyelination with an artificial external agent (*31*, *32*). Although many drugs that show efficacy in MS mouse models do not make it to the clinic, current drugs used to treat MS were developed on the basis of these models (*33*). It would be useful to test our compounds in other MS animal models, for example, using Semliki Forest virus and Theiler's murine encephalomyelitis virus to initiate an autoimmune reaction (*34*). We focused on the cuprizone model because it uses a toxin-based demyelination approach, and we had previous data demonstrating the efficacy of blocking excitotoxicity in mouse MS models (*24*).

ZCAN262 treatment rescued oligodendrocyte numbers but not to control levels. Possible explanations include that the small molecule is primarily acting to reduce neuron death and the subsequent release of myelin that in turn activates autoimmune attacks that kill more neurons and propagate the cycle. This mechanism of drug action will reduce the loss of myelin, whereas the production of myelin is by oligodendrocytes. The net amount of myelin is an equilibrium between production and destruction, and our drug works primarily on the latter. Another possibility is that we quantified oligodendrocyte markers too early in the recovery process and that additional serial measurements might capture more complete rescue.

In conclusion, MS remains a considerable therapeutic challenge, particularly the progressive forms of the disease for which there are limited treatments. The solution may be to move beyond immune-modulating drugs to a different strategy, and that is what our data support: a focus on protecting neurons and myelinated axons. Of

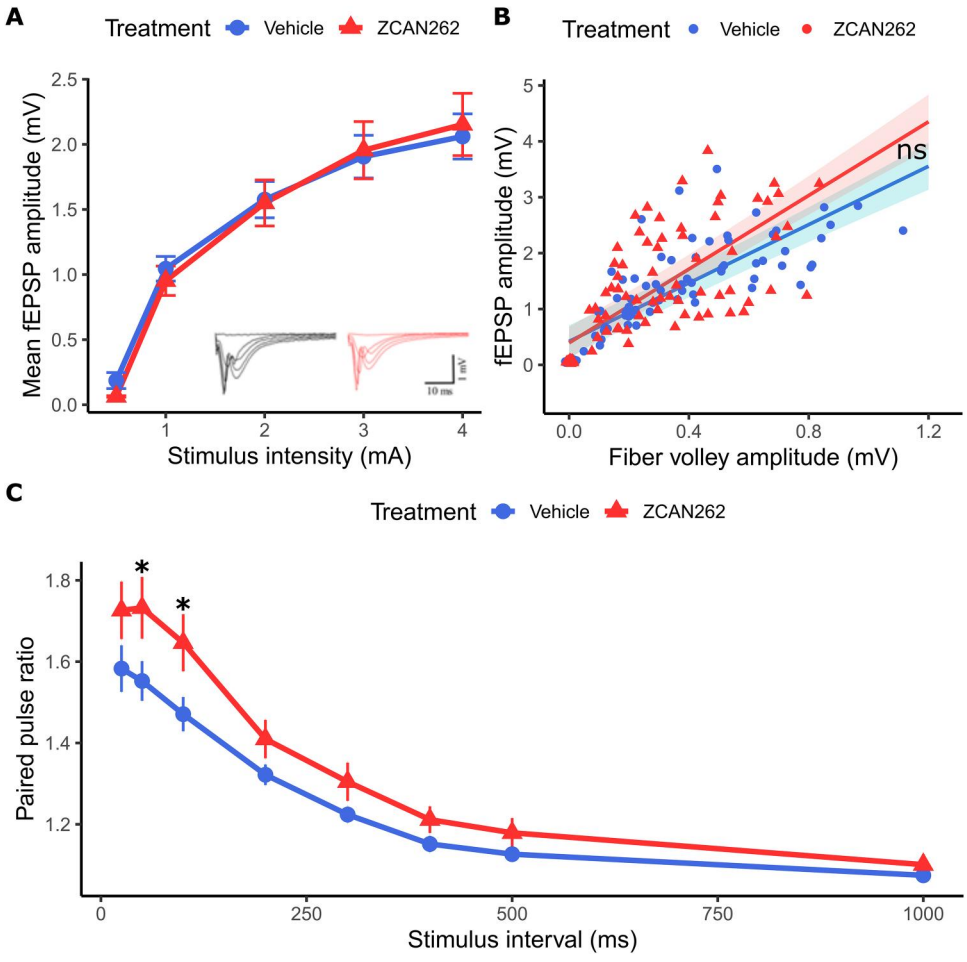

Fig. 8. Acute ZCAN262 treatment does not affect basal synaptic properties in hippocampus Schaffer collaterals. (**A**) fEPSP peak amplitude at varying stimulus intensities with example traces inset. (**B**) Input/output relationship showing fEPSP peak amplitude plotted against mean fiber volley amplitude at each stimulus intensity, general linear mixed effects model (GLM). (**C**) PPF expressed as the ratio between the second and first responses to two stimuli given at varying time intervals. Error bars indicate the means ± SEM, $n = 16$ measured brain slices taken from four mice, repeated-measures ANOVA or GLM, post hoc marginal means; ns, not significant; $^*P < 0.05$.

course, our data provide only the scientific starting point for drug development and, in addition to the experiments discussed above, will require substantial investment to collect basic data on toxicity, absorption, distribution, metabolism, and excretion, while simultaneously generating clinically applicable formulations, before human clinical trials can be attempted. Nevertheless, the data presented here suggest the potential for an MS treatment targeting AMPA-mediated excitotoxicity with a small-molecule allosteric modulator.

MATERIALS AND METHODS

In silico small-molecule screening

Small-molecule screening was performed by Atomwise using their AtomNet three-dimensional (3D) convolutional neural network for structure-based drug design (*28*). Data consisted of a 3D Cartesian coordinate mapping of each protein-ligand complex in multiple orientations, subsequently rasterized onto a grid based on the structural features present at each point. These grids formed the input for the 3D convolutional neural network. AtomNet was trained to predict binding affinity with a dataset of several million Ki and IC_{50} values and several thousand protein structures of different families using a network architecture of a 20 Å by 20 Å by 20 Å grid with a 1-Å spacing for the input layer, followed by four convolutional layers of 128 × 53, 256 × 33, 256 × 33, and 256 × 33 (number of filters × filter dimension), and two fully connected layers with 1024 rectified linear unit (ReLU) hidden units each (*28*), topped by a logistic-regression cost layer over two activity classes. Multiple poses within the binding site cavity for a given ligand were sampled. Each of these poses represents a putative co-complex. The scores for each pose in the ensemble were combined through weighted Boltzmann averaging to produce a final score. The error in these scores against experimentally measured Ki or IC_{50} values of protein-ligand pairs in the training set was minimized using stochastic gradient descent with the AdaDelta adaptive learning method (*35*), backpropagation (*36*), and mini-batches of 768 examples per gradient step.

The structure for AMPA glutamate receptor subunit 2 (GluA2) was downloaded from the PDB (3KG2), which contained the discovered N-terminal binding site (YYQWDKFAYLYDSDRGLSTLQAVLDSAAEK). The structure was inspected to ensure no missing residues in the binding site. Chimera was used to remove water molecules, add missing side chains and hydrogens, and relax steric strains via local energy minimization (*37*). The trained

AtomNet algorithm was used to predict scores for immediately commercially available compounds from the ZINC catalog. Salts and duplicate structures were filtered out along with molecules likely to cause assay artifacts chosen by applying pan-assay interference compounds (PAINS) filters to remove aggregators (*38*), autofluorescers, redox cyclers, or other problematic compounds that would interfere with the assay. Lipinski-like rules were used to filter out molecules that were predicted not to permeate the blood-brain barrier [$50 < M_W < 450$ daltons, cLogP < 5, topological polar surface area (TPSA) < 70, hydrogen bond donor (HBD) < 4, HB acceptor (HBA) < 8, number of chiral centers < 4] (*39*). Molecules remaining in the screen were clustered using the Butina algorithm and a Tanimoto similarity cutoff of 0.9 over the daylight fingerprints (*40*) implemented in OpenBabel (*41*). Exemplar compounds from each cluster were then ranked by AtomNet to screen for compounds that bind to the allosteric pocket.

Glutamate excitotoxicity cell death assay

Compounds were assessed for the prevention of glutamate-mediated excitotoxicity using CellTox Green cytotoxicity assay kits (Promega, G8743) following the manufacturer's instructions. HEK293 cells stably expressing GluA1 and GluA2 at a 1:1 ratio (Life Technologies Corporation, Carlsbad, CA, USA, SKU: M3771, custom order) were grown in Dulbecco's modified Eagle's medium with 10% fetal bovine serum. Cells were trypsinized and suspended in 0.05% EDTA-Trypsin. CellTox Green was added to the cell suspension (1:500 final volume), and 20 μl of the suspension was pipetted into the assay plates. The appropriate concentration of each test compound (highest concentration of 1 μM with a 3× serial dilution) was added to each well along with 10 μM AMPA, and the plates were incubated for 24 hours. Fluorescence intensity at 485 to 500 nm_{Ex}/520 to 530 nm_{Em} was then measured using a plate reader to assess cell death. Untreated and AMPA-only wells were included as positive and negative controls, respectively, along with 4 μl of CellTox green lysis solution alone to track assay drift. A dose-response curve was generated for compounds with an IC_{50} of less than 200 nM.

In vitro pharmacokinetics and toxicology

In vitro ADMET assays were conducted by Cyprotex Ltd. (U.K.) using industry-standard routine assay conditions described at https://cyprotex.com.

In vivo pharmacokinetics

Pharmacokinetics studies were conducted by Sai Life Sciences (India). Briefly, plasma pharmacokinetics and brain distribution of ZCAN262 were investigated in male Sprague Dawley rats following a single intravenous and oral administration at a dose of 5 mg/kg. Fifty-four male rats were divided into two groups as group 1 (n = 27) and group 2 (n = 27) with three rats per time point sparse sampling design. Animals in group 1 were administered intravenously as slow bolus injection through the tail vein, with solution formulation of ZCAN262 at a 5 mg/kg dose. Animals in group 2 were administered through the oral route with solution formulation of ZCAN262 at a 5 mg/kg dose. The formulation vehicle for both the groups was 5% v/v N-Methyl-2-pyrrolidone (NMP), 5% v/v Solutol HS-5, and 90% v/v normal saline. Blood samples (approximately 120 μl) were collected under light isoflurane anesthesia (Surgivet) from retro-orbital plexus from a set of three rats at predose (oral route of administration only), 0.08 (for intravenous only), 0.25, 0.5, 1, 2, 4, 6, 8, and 24 hours. In addition, along with terminal blood samples, brain samples were collected at pre-dose (for per os only), 0.08 (for intravenous only), 0.25, 0.5, 1, 2, 4, 6, 8, and 24 hours after dosing from three rats per time point. Immediately after blood collection, plasma was harvested by centrifugation at 4000 rpm, 10 min at 4°C, and samples were stored at −70 ± 10°C until bioanalysis. Following blood collection, immediately, the animals were euthanized, then abdominal vena cava was cut open, and the whole body was perfused from the heart using 10 ml of normal saline. Brain samples were collected from a set of three rats at each specified time point from respective animals. After isolation, tissue samples were rinsed three times in ice-cold normal saline (for 5 to 10 s/rinse using ~5 to 10 ml of normal saline in a disposable petri dish for each rinse) and dried on blotting paper. Tissue samples were homogenized using ice-cold phosphate-buffered saline (PBS, pH 7.4). Total homogenate volume was three times the tissue weight. All homogenates were stored below −70 ± 10°C until bioanalysis.

All samples were processed for analysis by protein precipitation method and analyzed with fit-for-purpose liquid chromatography tandem mass spectrometry method (LLOQ = 1.02 ng/ml for plasma and brain). The plasma and brain pharmacokinetic parameters were estimated using the noncompartmental analysis tool of Phoenix WinNonlin software (ver. 8.0).

Animals

All animal procedures were approved by the Center for Addiction and Mental Health Animal Care Committee and done in accordance with the requirements of the Province of Ontario Animals for Research Act 1971 and the Canadian Council on Animal Care. Mice were housed up to five per cage under controlled conditions (cellulose pellet bedding, Bed-r'Nest paper nesting, 23 ± 1°C, 50% ± 10% humidity, and 12-hour light cycle) with ad libitum access to food and water. C57BL/6 mice were ordered from Charles River Laboratories (Wilmington, MA, USA, stock no.: 027) and allowed to acclimate to the facility for 1 week and habituated to handling before the start of procedures.

Experimental autoimmune encephalitis

EAE was induced as described previously (*33*). Female C57BL/6 mice (9 weeks of age) were immunized by subcutaneous injection with recombinant $MOG_{35–55}$ (200 μg, Biomatik Corporation, Cambridge, ON, Canada) emulsified in complete Freund's adjuvant (incomplete Freund's adjuvant, Sigma-Aldrich, Oakville, ON, Canada; 4 mg/ml *Mycobacterium tuberculosis*, strain H37Ra, BD Biosciences, Missisauga, ON, Canada) into four sites on the back (50 μl per site). Pertussis toxin (200 ng, List Biological Laboratories Inc., Campbell, CA, USA) was injected intraperitoneally on days 0 and 2 after immunization. Mice were assessed daily using a scale for clinical signs of progressive paralysis [clinical score: 0, asymptomatic; 0.5, distal paresis of the tail; 1, complete tail paralysis; 1.5, paresis of the tail and mild hindlimb paresis; 2, unilateral severe hindlimb paresis; 2.5, bilateral severe hindlimb paresis; 3, complete bilateral hindlimb paralysis; 3.5 complete bilateral hindlimb paralysis and paresis of one front limb; 4, complete paralysis (tetraplegia)]. Animals were treated daily by intraperitoneal injection with compound **1** or compound **3**, or orally with ZCAN262 or vehicle [saline, 5% dimethyl sulfoxide (DMSO), and 5% Tween 80] via

oral gavage starting on day 11 after EAE induction, which is when symptoms first begin to appear.

Cuprizone-diet demyelination

High-protein control diet and 0.2% cuprizone diet were purchased from Envigo (Indianapolis, IN, USA). Female C57BL/6 mice (7 weeks of age) were switched from their standard diet to either the cuprizone or control diet for 6 weeks. Animals were then treated daily with ZCAN262 (5 mg/kg) or vehicle (saline, 5% DMSO, and 5% Tween 80) starting after 2 weeks on the cuprizone diet. After 6 weeks, the animals were subjected to behavioral testing and then euthanized for myelin assessment.

Transmission electron microscopy

Brains from control-diet or treated and untreated cuprizone-fed mice were prepared using the standard methods for the Embed 812 resin kit (Electron Microscopy Sciences, EMS). The corpus callosum was dissected from mice that were perfused with fixative. Samples were fixed with for 1 hour at room temperature (RT) and overnight at 4°C [4% paraformaldehyde (PFA) and 1% glutaraldehyde in 0.1 M phosphate buffer, pH 7.2]. Samples were washed 3× for 15 min each at RT (0.1 M phosphate buffer, pH 7.2) and then immersed in secondary fixative for 1 hour at RT in the dark (1% OsO_4 in 0.1 M phosphate buffer). Samples were washed three more times for 10 min at RT. Samples were then dehydrated in a gradient ethanol series: 30% for 15 min, 50% for 20 min, 70% for 30 min, 90% for 45 min, and 100% for 60 min. Samples were infiltrated using the Embed 812 resin kit (EMS) diluted with propylene oxide: 100% propylene oxide for 20 min, 33% (v/v) Embed 812 resin mixture in propylene oxide for 2 hours, 67% (v/v) for 3 hours, 100% Embed 812 overnight, and fresh 100% Embed 812 for 2 hours. After infiltration, samples in resin were put in molds and cured at 65°C for 48 hours.

Resin blocks were sectioned with a Reichert Ultracut E microtome (Leica) to 80-nm thickness and collected on 300 mesh copper grids (EMS). The sections were counter stained using saturated 5% uranyl acetate (EMS) for 10 min followed by Reynold's lead citrate (EMS) for 10 min. Prepared grids were placed on a filter paper mat in labeled petri dishes and stored in a desiccator until imaging. Sections were imaged using a Talos L120C transmission electron microscope (Thermo Fisher Scientific) at an accelerating voltage of 120 kV. Regions of interest were examined at magnifications from 2600× to 57,000× resulting in a field of view of 22.4 down to 1.02 μm, and a pixel size of 5.46 nm down to 249 pm. The density of myelinated axons was calculated as myelinated axon number per 100 μm^2. Myelin thickness was calculated as the outer diameter − inner diameter. g ratio was calculated as the inner diameter/outer diameter.

Immunohistochemistry

Mice were perfused with ice-cold PBS, followed by 4% PFA in PBS after anesthetic overdose. Brain tissue was postfixed in 4% PFA overnight and then transferred to 30% sucrose and frozen at −80°C. Coronal sections were cut using cryostat (25 μm). Sections were permeabilized with 0.3% Triton X-100 in PBS for 30 min and blocked with 2% bovine serum albumin in PBS at RT for 1.5 hours. Sections were incubated with anti-olig2 (1:200, Abcam, catalog ab109186), anti-Iba1 antibody (1:200, Novus, catalog NB100-1028), anti-Neurofilament nonphosphorylated (SMI-32, 1:200, BioLegend, catalog 837904), or anti-NeuN (1:200, Millipore, catalog MAB377) overnight at 4°C. Secondary antibodies were probed for 1.5 hours at RT. For FluoroMyelin Green staining, sections were incubated in staining solution (1:300, Invitrogen, catalog F34651) for 20 min at RT. All images were acquired using an Olympus FluoView FV1200 confocal microscope at ×10 magnification. The mean intensity of fluorescence signal was analyzed using ImageJ.

Electrophysiology

Male C57BL6/J mice were treated with ZCAN262 (5 mg/kg) or vehicle via oral gavage 1 hour before they were euthanized for electrophysiological recordings. Electrophysiological recordings were done in the Schaffer collateral-commissural pathway in the dorsal hippocampus as previously described. In brief, mouse brains were collected and prepared into 350-μm slices in ice-cold artificial cerebrospinal fluid (ACSF) saturated with 95% O_2/5% CO_2 [ACSF (mM): 120.0 NaCl, 3.0 KCl, 1.2 $MgSO_4$, 1.0 NaH_2PO_4, 26.0 $NaHCO_3$, 2.0 $CaCl_2$, and 11.0 D-glucose]. Prepared slices were allowed to recover at RT for at least 2 hours before the start of recording. Single slices were transferred to a submersion chamber and perfused with 95% O_2/5% CO_2 saturated ACSF maintained at 2.4 ml/min. Synaptic transmission was evoked by electrical stimulation at 0.067 Hz and recorded with glass pipettes (3 to 4 megohms) filled with ACSF. For the input-output field potential recordings, the stimulus intensity was increased gradually (0, 1, 2, 3, 4, and 5 mA). For PPF, stimulation was delivered with inter-pulse intervals of 25, 50, 100, 200, 300, 400, 500, or 1000 ms, and PPF was calculated as the ratio of the second response peak value over the first.

Behavioral testing

Open field test

The open field test procedure was performed using Noldus PhenoTyper boxes, which consist of 30 cm by 30 cm by 35 cm (length by width by height) plexiglass chambers with built-in infrared camera and lighting systems. Mice were placed in the PhenoTypers and recorded for a 90-min period. Velocity and distance traveled were scored automatically using Ethovision XT software.

Rotarod

A Panlab rotarod apparatus was used for the rotarod test. Mice were placed on the apparatus and allowed to walk for 1 min with the tracks rotating at 4 rpm. The rotation speed was then accelerated from 4 to 40 rpm over 120 s. The time and rpm at the fall was measured and averaged over three trials for each mouse.

Novel object recognition test

The NORT was performed as previously described (*42*). The procedure consisted of a habituation phase, familiarization phase, and a novelty phase. During habituation, each mouse was allowed to freely explore the empty open field arena (40 cm by 40 cm by 40 cm) for 5 min. During familiarization the following day, two identical objects (blue bottle caps) were placed near the two corners at either end of one side of the arena, and each mouse was placed into the arena and allowed to explore freely for 5 min. After a 1-hour delay, either the left or right familiar object was replaced with a novel object (T-25 flask filled corn cob bedding) for the novelty phase, alternating for each mouse. Mice were placed into the arena and allowed to explore freely for 5 min. The time spent investigating each object was recorded (nose within 2 cm of the object) and scored using Ethovision 10 software. The DI was calculated for the novelty phase as [DI = (Novel − Familiar)/(Novel + Familiar)]. Male C57BL/6 mice were

treated daily with ZCAN262 (5 mg/kg) or vehicle via oral gavage starting 1 week before testing.

Morris water maze

The MWM was performed as previously described (*43*). The MWM consisted of a 100-cm diameter pool with a 10-cm diameter platform submerged in water tinted with nontoxic tempura paint. Mice were placed in the MWM at differing starting positions approximately equidistant from the platform and given 60 s to find the platform on each trial. Each mouse underwent six trials per day separated by 20 min. On the pretraining day, mice were trained with the platform visible. The mice were then trained for 4 days in the MWM. The mean time it took to find the platform across all trials on each training day was recorded and analyzed with Ethovision 10 software. Male C57BL/6 mice were treated daily with ZCAN262 (5 mg/kg) or vehicle via oral gavage starting 1 week before testing.

Statistical analysis

Data were checked for normality with Shapiro's test and homogeneity of variance with Bartlett's test. Residual plots were examined for normality and homoscedasticity. Pairwise means were compared with Welch's *t* tests. Factorial data from histology and biochemistry experiments were analyzed by one-way analysis of variance (ANOVA) with post hoc Tukey's, Dunnett's, or marginal means contrasts where indicated. Repeated-measures ANOVAs were used for EPSP amplitude, PPF, and time-series data (e.g., EAE clinical score, and MWM). False discovery rate was used for multiple-test correction for sets of contrasts. Fixed-slopes linear regression was used to compare g ratio against axon diameter. General linear mixed effect models were used for input/output analysis with fEPSP amplitude as a response, fiber volley amplitude and treatment as predictors, measured brain slice as a random effect, and stimulus intensity as a covariate. Outliers were removed by detecting points with all three of Mahalanobis distance, Cook's distance, and leverage above the calculated thresholds (degrees of freedom per sample). Multicollinearity was detected by calculating variance inflation factors. Autocorrelation was tested using Durbin-Watson tests. Confidence intervals were calculated by bootstrap resampling where shown. Analyses were performed using Graphpad Prism or R.

Supplementary Materials

This PDF file includes:
Figs. S1 to S3
Table S1
Legend for data S1

Other Supplementary Material for this manuscript includes the following:
Data S1

REFERENCES AND NOTES

1. R. W. Orrell, Multiple sclerosis: The history of a disease. *J Roy Soc Med* **98**, 289–289 (2005).
2. M. S. Kaller, A. Lazari, C. Blanco-Duque, C. Sampaio-Baptista, H. Johansen-Berg, Myelin plasticity and behaviour—Connecting the dots. *Curr. Opin. Neurobiol.* **47**, 86–92 (2017).
3. A. Compston, A. Coles, Multiple sclerosis. *Lancet* **372**, 1502–1517 (2008).
4. R. A. Marrie, Environmental risk factors in multiple sclerosis aetiology. *Lancet Neurol.* **3**, 709–718 (2004).
5. J. F. Kurtzke, A. Heltberg, Multiple sclerosis in the Faroe islands. *J. Clin. Epidemiol.* **54**, 1–22 (2001).
6. K. Bjornevik, M. Cortese, B. C. Healy, J. Kuhle, M. J. Mina, Y. Leng, S. J. Elledge, D. W. Niebuhr, A. I. Scher, K. L. Munger, A. Ascherio, Longitudinal analysis reveals high prevalence of Epstein-Barr virus associated with multiple sclerosis. *Science* **375**, 296–301 (2022).
7. E. C. Leibovitch, S. Jacobson, Evidence linking HHV-6 with multiple sclerosis: An update. *Curr. Opin. Virol.* **9**, 127–133 (2014).
8. M. Torabi, C. Green, N. Yu, R. A. Marrie, Application of three focused cluster detection methods to study geographic variation in the incidence of multiple sclerosis in Manitoba, Canada. *Neuroepidemiology* **43**, 38–48 (2014).
9. E. Kamma, W. Lasisi, C. Libner, H. S. Ng, J. R. Plemel, Central nervous system macrophages in progressive multiple sclerosis: Relationship to neurodegeneration and therapeutics. *J. Neuroinflammation* **19**, 45 (2022).
10. N. A. Patsopoulos, Genetics of multiple sclerosis: An overview and new directions. *Cold Spring Harb. Perspect. Med.* **8**, (2018).
11. S. Sawcer, R. J. M. Franklin, M. Ban, Multiple sclerosis genetics. *Lancet Neurol.* **13**, 700–709 (2014).
12. W. Kim, N. A. Patsopoulos, Genetics and functional genomics of multiple sclerosis. *Semin. Immunopathol.* **44**, 63–79 (2022).
13. M. Filipi, S. Jack, Interferons in the treatment of multiple sclerosis: A clinical efficacy, safety, and tolerability update. *Int J MS Care* **22**, 165–172 (2020).
14. A. Kasindi, D.-T. Fuchs, Y. Koronyo, A. Rentsendorj, K. L. Black, M. Koronyo-Hamaoui, Glatiramer acetate immunomodulation: Evidence of neuroprotection and cognitive preservation. *Cell* **11**, (2022).
15. P. S. Rommer, R. Milo, M. H. Han, S. Satyanarayan, J. Sellner, L. Hauer, Z. Illes, C. Warnke, S. Laurent, M. S. Weber, Y. Zhang, O. Stuve, Immunological aspects of approved MS therapeutics. *Front. Immunol.* **10**, 1564 (2019).
16. S. Faissner, J. R. Plemel, R. Gold, V. W. Yong, Progressive multiple sclerosis: From pathophysiology to therapeutic strategies. *Nat. Rev. Drug Discov.* **18**, 905–922 (2019).
17. B. D. Trapp, K.-A. Nave, Multiple sclerosis: An immune or neurodegenerative disorder? *Neuroepidemiology* **31**, 247–269 (2008).
18. A. Cianfoni, S. Niku, S. G. Imbesi, Metabolite findings in tumefactive demyelinating lesions utilizing short echo time proton magnetic resonance spectroscopy. *AJNR Am. J. Neuroradiol.* **28**, 272–277 (2007).
19. P. Sarchielli, L. Greco, A. Floridi, A. Floridi, V. Gallai, Excitatory amino acids and multiple sclerosis: Evidence from cerebrospinal fluid. *Arch. Neurol.* **60**, 1082–1088 (2003).
20. J. Newcombe, A. Uddin, R. Dove, B. Patel, L. Turski, Y. Nishizawa, T. Smith, Glutamate receptor expression in multiple sclerosis lesions. *Brain Pathol.* **18**, 52–61 (2008).
21. D. Centonze, L. Muzio, S. Rossi, F. Cavasinni, V. D. Chiara, A. Bergami, A. Musella, M. D'Amelio, V. Cavallucci, A. Martorana, A. Bergamaschi, M. T. Cencioni, A. Diamantini, E. Butti, G. Comi, G. Bernardi, F. Cecconi, L. Battistini, R. Furlan, G. Martino, Inflammation triggers synaptic alteration and degeneration in experimental autoimmune encephalomyelitis. *J. Neurosci.* **29**, 3442–3452 (2009).
22. G. Sulkowski, B. Dąbrowska-Bouta, M. Chalimoniuk, L. Strużyńska, Effects of antagonists of glutamate receptors on pro-inflammatory cytokines in the brain cortex of rats subjected to experimental autoimmune encephalomyelitis. *J. Neuroimmunol.* **261**, 67–76 (2013).
23. M. Wang, S. Li, H. Zhang, L. Pei, S. Zou, F. J. S. Lee, Y. T. Wang, F. Liu, Direct interaction between GluR2 and GAPDH regulates AMPAR-mediated excitotoxicity. *Mol. Brain* **5**, 13 (2012).
24. D. Zhai, F. H. F. Lee, C. D'Souza, P. Su, S. Zhang, Z. Jia, L. Zhang, A. H. C. Wong, F. Liu, Blocking GluR2-GAPDH ameliorates experimental autoimmune encephalomyelitis. *Ann. Clin. Transl. Neurol.* **2**, 388–400 (2015).
25. R. Roesler, J. Quevedo, N. Schröder, Is it time to conclude that NMDA antagonists have failed? *Lancet Neurol.* **2**, 13; discussion 13 (2003).
26. T. Reuillon, S. E. Ward, P. Beswick. Modulating AMPA receptors for the treatment of CNS disorders, in *Comprehensive Medicinal Chemistry III* (Elsevier Ltd., 2017), pp. 447–480.
27. I. H. Greger, J. F. Watson, S. G. Cull-Candy, Structural and functional architecture of AMPA-Type glutamate receptors and their auxiliary proteins. *Neuron* **94**, 713–730 (2017).
28. I. Wallach, M. Dzamba, A. Heifets, AtomNet: A deep convolutional neural network for bioactivity prediction in structure-based drug discovery. arXiv:1510.02855 [cs.LG] (10 October 2015).
29. M. Cercignani, G. Giulietti, N. G. Dowell, M. Gabel, R. Broad, P. N. Leigh, N. A. Harrison, M. Bozzali, Characterizing axonal myelination within the healthy population: A tract-by-tract mapping of effects of age and gender on the fiber g-ratio. *Neurobiol. Aging* **49**, 109–118 (2017).
30. R. S. Zucker, W. G. Regehr, Short-term synaptic plasticity. *Annu. Rev. Physiol.* **64**, 355–405 (2002).

31. C. S. Constantinescu, N. Farooqi, K. O'Brien, B. Gran, Experimental autoimmune encephalomyelitis (EAE) as a model for multiple sclerosis (MS). *Br. J. Pharmacol.* **164**, 1079–1106 (2011).
32. G. K. Matsushima, P. Morell, The neurotoxicant, cuprizone, as a model to study demyelination and remyelination in the central nervous system. *Brain Pathol.* **11**, 107–116 (2001).
33. D. Baker, S. Amor, Mouse models of multiple sclerosis: Lost in translation? *Curr. Pharm. Des.* **21**, 2440–2452 (2015).
34. B. J. van der Star, D. Y. S. Vogel, M. Kipp, F. Puentes, D. Baker, S. Amor, In vitro and in vivo models of multiple sclerosis. *CNS Neurol. Disord. Drug Targets* **11**, 570–588 (2012).
35. M. D. Zeiler, ADADELTA: An adaptive learning rate method. arXiv:1212.5701v1 [cs.LG] (22 December 2012).
36. D. E. Rumelhart, G. E. Hinton, R. J. Williams, in *Neurocomputing: Foundations of Research*, J. A. Anderson, E. Rosenfeld, Eds. (MIT Press, 1988), pp. 696–699.
37. E. F. Pettersen, T. D. Goddard, C. C. Huang, G. S. Couch, D. M. Greenblatt, E. C. Meng, T. E. Ferrin, UCSF Chimera–A visualization system for exploratory research and analysis. *J. Comput. Chem.* **25**, 1605–1612 (2004).
38. J. B. Baell, G. A. Holloway, New substructure filters for removal of pan assay interference compounds (PAINS) from screening libraries and for their exclusion in bioassays. *J. Med. Chem.* **53**, 2719–2740 (2010).
39. H. Pajouhesh, G. R. Lenz, Medicinal chemical properties of successful central nervous system drugs. *NeuroRx* **2**, 541–553 (2005).
40. M. Sastry, J. F. Lowrie, S. L. Dixon, W. Sherman, Large-scale systematic analysis of 2d fingerprint methods and parameters to improve virtual screening Enrichments. *J. Chem. Inf. Model.* **50**, 771–784 (2010).
41. N. M. O'Boyle, M. Banck, C. A. James, C. Morley, T. Vandermeersch, G. R. Hutchison, Open babel: An open chemical toolbox. *J. Chem.* **3**, 33 (2011).
42. M. Leger, A. Quiedeville, V. Bouet, B. Haelewyn, M. Boulouard, P. Schumann-Bard, T. Freret, Object recognition test in mice. *Nat. Protoc.* **8**, 2531–2537 (2013).
43. S. J. Clapcote, N. L. Lazar, A. R. Bechard, J. C. Roder, Effects of the rd1 mutation and host strain on hippocampal learning in mice. *Behav. Genet.* **35**, 591–601 (2005).

Acknowledgments

Funding: This research was supported by the following grants: a Centre for Addiction and Mental Health Foundation Proof of Principle grant held by F.L., a Canadian Institute of Health Research Proof of Principle Phase II grant held by F.L. and I.R.G., and funding from the National Multiple Sclerosis Society (USA) Fast-Forward Commercialization Program held by F.L. and I.R.G.

Author contributions: Conceptualization: D.Z., I.R.G., and F.L. Methodology: D.Z., S.Y., J.S., L.W., P.S., H.Z., Z.J., I.W., A.H., C.Z., and C.-C.T. Investigation: D.Z., S.Y., J.S., L.W., P.S., A.J., H.Z., I.W., A.H., C.Z., and C.-C.T. Visualization: D.Z., S.Y., J.S., P.S., H.Z., C.Z., and C.-C.T. Formal analysis: D.Z., S.Y., and J.S. Funding acquisition: I.R.G. and F.L. Supervision: Z.J., A.H.C.W., I.R.G., and F.L. Writing—original draft: J.S., A.H.C.W., and I.R.G. Writing—review and editing: J.S., A.H.C.W., I.R.G., and F.L.

Competing interests: Pending patent applications entitled "Modulators of ampa receptor signaling" have been filed in US (17/310,996), CA (3,132,446), EP (20766043.2), HK (62022056472.3), AU (2020231118), and CN (202080033793.0), with international publication number WO2020/178782, protecting the small molecules discussed herein. The coinventors include F.L., I.R.G., D.Z., C.Z., C.-C.T., and S. A. Smith. A.H. and I.W. are the CEO and CTO, respectively, and cofounders of Atomwise Inc., a technology startup using AI for small-molecule drug discovery. Methods used by Atomwise Inc. are protected under active patent number US10002312B2 entitled "Systems and methods for applying a convolutional network to spatial data" with coinventors A.H., I.W., and M. Dzamba. The authors declare that they have no other competing interests. **Data and materials availability:** The use of AtomNet for the virtual screen was purchased on a pay for service contract. All other data needed to evaluate the conclusions in the paper are present in the paper and/or the Supplementary Materials.

Submitted 7 July 2023
Accepted 9 November 2023
Published 8 December 2023
10.1126/sciadv.adj6187